RESEARCH PAPER

CrossMark

Modeling and experimental validation of friction self-piercing riveted aluminum alloy to magnesium alloy

YunWu Ma[1,2] · Ming Lou[1] · YongBing Li[1,2] · ZhongQin Lin[1,2]

Abstract

Friction self-piercing riveting (F-SPR) process has been proposed to achieve crack-free joining of low-ductility materials by combining SPR process with the concept of friction stir processing. The inhibition of cracking in an F-SPR joint is related to the in-process temperature as well as plastic deformation of materials, which are controlled by the process parameters, i.e., spindle speed and feed rate. However, the relationship between F-SPR process parameters and the temperature characteristics within the joint has not been established. In the current study, a coupled thermal-mechanical model based on solid mechanics was setup to study the F-SPR process of aluminum alloy and magnesium alloy. Temperature and strain rate-dependent material models and preset crack surface method were integrated in the model and geometry comparisons were conducted for model validation. Based on this model, the evolutions of temperature and plastic deformation in the rivet and the sheets of an F-SPR joint were obtained to reveal the formation mechanism of the joint. The temperature distribution and evolution of the sheet materials were correlated with F-SPR process parameters, and a critical spinning speed of 2000 rpm at a feed rate of 1.35 mm/s was determined capable of inhibiting cracking in the magnesium sheet.

1 Introduction

Replacing traditional steels with high strength-to-weight ratio materials is one of the main methods to achieve the lightweighting goals of vehicle bodies. Aluminum alloys are preferred lightweight materials for their high strength, low density, good corrosion resistance, and intrinsic recyclability, and have been widely used in full aluminum and aluminum-steel mixed material bodies [1]. Magnesium alloys are

---

✉ YongBing Li
   yongbinglee@sjtu.edu.cn

1   Shanghai Key Laboratory of Digital Manufacture for Thin-walled Structures, School of Mechanical Engineering, Shanghai Jiao Tong University, Shanghai 200240, People's Republic of China

2   State Key Laboratory of Mechanical System and Vibration, School of Mechanical Engineering, Shanghai Jiao Tong University, Shanghai 200240, People's Republic of China

extremely light metals and show even better lightweight performance than Al alloys [2]. Integrating Al and Mg alloys in one hybrid structure is more promising to achieve a flexible product design, which raises the demand of an economical and reliable Al-Mg dissimilar material joining process.

Resistance spot welding (RSW) process is the primary spot joining technology of steel parts in vehicle body assembling for its low cost and high speed. In recent years, RSW has also been successfully applied to join Al alloy parts by using an innovative electrode tip design [3]. However, when RSW is applied to weld Al and Mg alloys as well as other dissimilar metals, a major technological difficulty is the formation of hard and brittle intermetallic compound (IMC) layers at the interface, which has detrimental effect on both mechanical strength and fatigue life of the joint [4–6].

Self-piercing riveting (SPR) process is a preferred method to join dissimilar materials in vehicle industry, such as Al alloy and steel. In an SPR joint, a semi-tubed rivet is punched into the sheet materials and the rivet shank deformed plastically to form a mechanical interlocking with the sheets [7]. Mori et al. [8] joined multiple steel and aluminum alloy sheets with SPR. Ma et al. [9] investigated the effects of rivet and die properties

🖄 Springer

on joint formation and mechanical performance of SPRed Al alloy to steel joints. However, when SPR is applied to the stack-ups including materials having limited ductility at room temperature, such as Mg alloy and cast Al, especially used as the bottom layer, cracking occurs inevitably due to the severe localized plastic deformations in the SPR joint [10]. To achieve crack-free joining of Mg sheets, Durandet et al. [11] preheated the magnesium alloy AZ31 sheets with leaser prior to the SPR process. It was found that cracking in the Mg sheet can be eliminated when performing SPR at 208 °C. Wang et al. [12] preheated Mg sheets with electrical-heated plate before SPR and pointed that the preheating temperature of higher than 180 °C could avoid cracking. This is related to the hexagonal crystal in Mg alloy sheet, which only has three basal slip systems at room temperature, but additional non-basal slip systems in the crystal structure can be activated at elevated temperature to significantly improve the formability [13].

Friction self-piercing riveting (F-SPR) is a process with combination of friction stir process and SPR process, during which a semi-tubed rivet is driven to spin at a high speed while feeding into the workpieces [14] (refer to Fig. 1). The large amount of frictional heat generated at the periphery of the rotating rivet enables the riveting process to be finished at elevated temperature. In this way, in-process heating is realized and thus can significantly lower the process cycle time compared to preheating SPR technology. Li et al. [14] demonstrated that cracking in Mg sheet was able to be inhibited through adjusting the spindle speed and feed rate during F-SPR process. The tensile shear strength of an F-SPRed Al-Mg joint was found twice as much as that of an SPR joint. Ma et al. [15] optimized the F-SPR rivet in terms of key geometrical features and hardness. Liu et al. [16] conducted the F-SPR process on a specially designed machine that could achieve sudden stop of the spindle to further improve the joint quality. Ma et al. [17] established a coupled thermo-mechanical finite element (FE) model to visualize the evolution of joint geometry, stress, and strain distributions inside the F-SPR joint. Similar combinations of friction stir process and riveting process were also reported by Min et al. [18] and Han et al. [19] in joining Al to Mg and Mg to itself, respectively.

As reviewed above, cracking inhibition in Mg sheet during F-SPR process is related to the amount of local frictional heat

generation, which is controlled by the process parameters, i.e., the spindle speed and the feed rate. However, limited by experimental observation means, it is difficult to observe the in-process temperature and deformation of materials within the vicinity of the rotating rivet. Therefore, the relationship between process parameters and the temperature of workpieces during F-SPR process has not been established.

In the present study, a coupled thermo-mechanical 3D FE model of the F-SPR process, based on solid mechanics, was established and validated through geometry comparison with the parallel physical testing results. Based on this model, the effects of process parameters on the temperature distribution and evolution during the F-SPR process were studied systematically and a critical spinning speed to inhibit cracking in the Mg sheet was determined. The method and results in this study provide a valuable reference to F-SPR process optimization.

2 Mathematical model
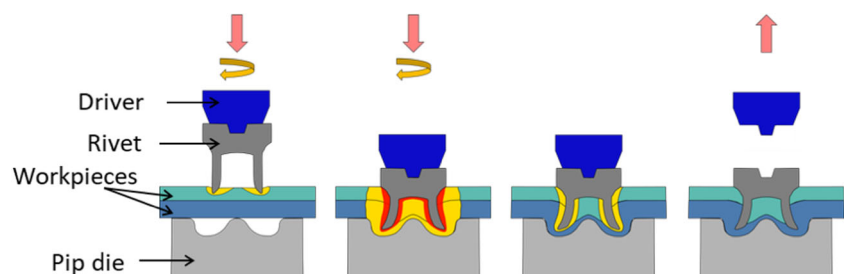
2.1 Governing equations

F-SPR is a coupled thermo-mechanical process, which involves both mechanical movement and thermal response. The mechanical motion is governed by the differential equation of motion, which in the general form of a force balance is given by

$$\rho\ddot{u} + c\dot{u} + ku = f \tag{1}$$

where ρ, c, and k are the density, the damping coefficient per unit volume, and the stiffness coefficient per unit volume, respectively. u is the the displacement vector and f is the body force per unit volume.

Frictional work and plastic dissipation energy are considered as the two heat sources in F-SPR process and treated, respectively, as a surface heat influx at the rivet/workpiece interface and a body heat source in the plastically deformed materials. The thermal response in a unit volume is governed by the general thermomechanical diffusion equation [20], given as

Fig. 1 Schematic of the friction self-piercing riveting process

Driver
Rivet
Workpieces
Pip die

$$\rho c_p \frac{\partial T}{\partial t} = \frac{\partial}{\partial x}\left[k_x \frac{\partial T}{\partial x}\right] + \frac{\partial}{\partial y}\left[k_y \frac{\partial T}{\partial y}\right] + \frac{\partial}{\partial z}\left[k_z \frac{\partial T}{\partial z}\right] + Q \quad (2)$$

where ρ is the material density, c_p is the specific heat capacity, k_x, k_y, and k_z are the thermal conductivities in different directions, T is temperature, t is time, and Q is the internal heat generation rate per unit volume. The volumetric heat flux Q is calculated as

$$Q = \eta \sigma \dot{\varepsilon} \quad (3)$$

where η is the fraction of plastic energy converted to heat, σ is the flow stress, and $\dot{\varepsilon}$ is the strain rate, which is in the form of von Mises equivalent strain rate in this study, given by

$$\dot{\varepsilon} = \sqrt{\left(\frac{2}{3} e_{ij} e_{ij}\right)} \quad (4)$$

$$e_{ij} = \frac{1}{2}\left(\frac{\partial v_i}{\partial x_j} + \frac{\partial v_j}{\partial x_i}\right) \quad (5)$$

where v is velocity. The frictional heat influx at the interface is computed as

$$q_f = \beta v_{rel} \tau_f \quad (6)$$

where q_f is the frictional heat generation per unit area, β donates the fraction of frictional work converted to heat, v_{rel} is the magnitude of the relative tangential velocity at the interface, and τ_f is the local contact shear stress. v_{rel} is calculated as

$$v_{rel} = \left|\vec{v}_{master} - \vec{v}_{slave}\right| \quad (7)$$

where $\vec{v}_{master}$ and $\vec{v}_{slave}$ are the tangential velocity vectors of the master side and the slave side at the contact interface, respectively. It should be noted that a pure sliding contact condition, i.e., ignoring sticking at the rivet/workpiece interface, is assumed in the model. Therefore, the local contact shear stress is calculated as

$$\tau_f = \mu \sigma_n \quad (8)$$

where μ is the friction coefficient and σ_n is the interfacial normal stress at the specific contact location. This pure sliding assumption means plastic deformation of the sheet materials resulting from the rotation motion of the rivet is not considered, and the body heat flux Q only accounts for the heat generation of plastic deformation introduced by the feeding motion of the rivet. This assumption might be a disadvantage of the current model since sticking contact possibly exists as

the workpiece becomes soft with increase in temperature. Further study is needed to clarify the contact condition at the rivet/workpiece interface in F-SPR process.

The fraction of generated frictional heat partitioned to the contacting parts is calculated according to the relationship given by [21]

$$n_s = \frac{\sqrt{(k\rho c_p)_s}}{\sqrt{(k\rho c_p)_s} + \sqrt{(k\rho c_p)_m}} \quad (9)$$

where the subscripts s and m denote the slave side and the master side materials, respectively, n_s represents the fraction of heat partitioned to the slave side, and the fraction partitioned to the master side is given by

$$n_m = 1 - n_s \quad (10)$$

At the contacting surfaces, heat transfer from high-temperature end to low-temperature end is accounted as heat conduction between parts and the conducted heat is computed as

$$q_t = h(T_a - T_b) \quad (11)$$

where q_t is the heat transfer per unit square, h is heat transfer coefficient at the contacting surfaces, and T_a and T_b are the temperatures of the high-temperature and low-temperature ends, respectively.

2.2 Material constitutive and properties

Wang et al. [12] estimated that the sheet materials underwent a strain rate of about 4.1 s^{-1} at a riveting velocity of 110 mm/s during SPR process. The feed rate in F-SPR process ranges from 1 to 10 mm/s [14], which is about 1~9% of the riveting velocity in SPR. Therefore, the strain rate of sheet materials in F-SPR is approximately in the order of 0.01~0.1 s^{-1}. To consider strain rate and temperature-dependent material properties of the workpiece materials during F-SPR process, Johnson-Cook (J-C) constitutive model is adopted. The flow stress is a function of equivalent strain, strain rate, and temperature, given by [22]:

$$\sigma = \left(A + B\varepsilon_e^n\right)\left(1 + C\ln\frac{\dot{\varepsilon}}{\dot{\varepsilon}_0}\right)\left(1 - \left(\frac{T - T_{room}}{T_{melt} - T_{room}}\right)^m\right) \quad (12)$$

where ε_e is the effective plastic strain, $\dot{\varepsilon}$ and $\dot{\varepsilon}_0$ are the strain rate and reference strain rate ($\dot{\varepsilon}_0 = 1\ s^{-1}$), respectively, and T, T_{room}, and T_{melt} are the absolute testing, room, and melting temperatures, respectively. The material constant A represents

Table 1 Material constants of the Johnson-Cook law for AA6061-T6 and AZ31B

Material	A	B	C	n	m	T_{room}	T_{melt}
AA6061-T6 [23]	324	114	0.002	0.42	1.34	24 °C	583 °C
AZ31B [24]	224	380	0.012	0.76	1.55	20 °C	630 °C

the yield strength of the material. B and n are strain hardening-related constants. The strain rate effect and temperature effect are represented through constants C and m, respectively. Generally, quasi-static tensile tests are needed to determine the constants A, B, and n. High strain rate tensile tests are performed to determine strain rate sensitivity constant C. High-temperature tensile tests are performed to determine the temperature-related constant m. For the studied sheet materials, i.e., 1.0-mm-thick aluminum alloy AA6061-T6 and 2.2-mm-thick magnesium alloy AZ31B, the J-C model constants from literature are used [23, 24], as listed in Table 1. The temperature-dependent specific heat capacity and thermal conductivity of materials are given in Table 2. Since the values of density of these two materials change very slightly (less than 2% [23, 25]) with the increase of temperature from 20 to 300 °C, constant values of density are used. The material chemical compositions of sheet materials are listed in Table 3.

To simulate material failure of the top Al sheet during the F-SPR process, preset crack method is adopted. Crack surfaces are preset in the locations where fracture is likely to occur, i.e., the areas of the top sheet contacting with the rivet shank tip, and separation of the matting surfaces are triggered by the criteria [27] given as

$$\left[\frac{max(0,\ \sigma_{normal})}{FS}\right]^2 + \left[\frac{\sigma_{shear}}{FD}\right]^2 > 1 \qquad (13)$$

where σ_{normal} and σ_{shear} are the normal and shear stresses on the interfaces, and FS and FD are the predefined normal tensile stress at failure and shear stress at failure, respectively. Once Eq. (13) is reached at any region of the mating surfaces,

the nodes on both sides of the interface in this region would detach from each other. The normal tensile stress at failure of top sheet is set to be the ultimate tensile strength (σ_b) of AA6061-T6, which is temperature dependent (refer to Table 2). The shear stress at failure is set to be $\sigma_b/\sqrt{3}$.

The F-SPR rivet used in F-SPR experiments was made of mild steel and modified from commercial bolt rivet provided by Henrob Corporation [14]. Table 3 lists the chemical composition of the rivet. In view of the difficulties in measuring the mechanical properties of the steel rivets, compression tests of the rivet shank were conducted at room temperature and linear correlation between hardness and strength was used to calculate the material properties of the rivet at high temperatures. The material testing details and calculated material properties were presented in a previous work [17]. Constant thermal conductivity of 50 W/m·°C and specific heat capacity of 500 J/kg·°C were used for the rivet [21].

2.3 Numerical implementation

Figure 2a shows the geometry and mesh generation of the mathematical model. As shown, the five parts were the rivet driver, the steel rivet, the top AA6061-T6 sheet, the bottom AZ31B sheet, and the die, respectively, from the top to the bottom. The rivet driver and the die were defined as rigid bodies, while the rivet and sheets were defined as deformable bodies. The radius of the sheets was 9.0 mm and the thickness was 1.0 and 2.2 mm for AA6061-T6 and AZ31B, respectively. The meshes of sheets were carefully created such that a refined element distribution with a higher density was in the ring regions near the rivet shank tip, the average size of which was around $0.16 \times 0.2 \times 0.2$ mm. The specific dimensions of the rivet and the die were presented in literatures [14, 15]. The element size of the rivet is comparable with those in the refined region of the sheets. To accurately simulate the material failure of top sheet, five predefined crack surfaces were set in the regions of the top sheet that are located in the periphery of the rivet shank. Figure 3 gives the locations of the five

Table 2 Temperature-dependent material properties of AA6061-T6 and AZ31B

Material	Temperature (°C)	Density (kg/m³)	Thermal conductivity (W/m·°C)	Specific heat capacity (J/kg·°C)	Ultimate tensile strength (MPa)
AA6061-T6 [17, 23, 26]	20	2690	161.2	941.2	352.8
	100	2690	177.5	980.6	301.2
	200	2690	191.4	1026.3	236.53
	300	2690	205.6	1071.4	128.32
AZ31B [25]	20	1790	96.6	1050	–
	100	1790	100.5	1130	–
	200	1790	104.7	1170	–
	300	1790	108.9	1210	–

Table 3 Chemical composition of rivet, AA6061-T6, and AZ31B [14, 17]

Material type	Nominal chemical composition (wt%)									
	Al	Mg	Fe	C	Si	Cu	Mn	Zn	Cr	Ti
Rivet	0.02	–	Bal.	0.18	–	–	0.75	–	0.32	–
AA6061-T6	Bal.	1.03	0.14	–	0.58	0.32	0.07	0.03	0.08	0.05
AZ31B	3.05	Bal.	0.001	–	0.016	0.003	0.44	1.10	–	–

predefined cylindrical surfaces, which were evenly spaced with an interval of 0.16 mm.

In the model, the die was constrained in all degrees of freedom (DOF). The rivet driver was constrained to spin and translate only along the symmetry axis with predefined feed rate and spinning speed. In order to transfer driving torque to the rivet, nodes on top of the rivet contacting with the rivet driver were tied to the rivet driver (refer to Fig. 2b). In F-SPR experiments, blank holder was forced to the top surface of the upper sheet to prevent any gap formation between the two layers of sheets. In the numerical model, for simplicity, nodes within the outer ring-shaped portions of the two layers of sheets were constrained in all DOF, as highlighted in Fig. 2c. Nodes-to-surface contact were used by specifying the nodes of top sheet as the slave side and the surface of the rivet as the master side to prevent element penetration when the rivet pierced through the top sheet. For the rest of the contact pairs, surface-to-surface contact was used.

Convection and radiation heat loss from the surfaces to environment were not considered since the total processing time of F-SPR was short (less than 3.2 s). The heat transfer coefficients were assumed to be 500 W/m^2 K at all the contacting surfaces by referring to the existing research on modeling of friction stir welding (FSW) process [28, 29]. An initial temperature of 20 °C was assigned to all the parts. In the present study, it was assumed that all the frictional work and plastic energy were converted to heat, i.e., both η in Eq. (3) and β in Eq. (6) were assumed to be 1.0.

Friction coefficient is usually considered as a function of the relative velocity of mating surfaces and the interface temperature according to Coulomb friction model. However, during F-SPR, the coefficient can be highly nonlinear due to the involved large ranges of temperature and strain rate. Since no such a function is available from open literature for the studied rivet and sheet materials, the friction coefficient at all contact interfaces is fixed at 0.3, which is typical in modeling FSW process [28]. This assumption may result in the inaccuracy in calculated frictional heat generation at relative high temperature.
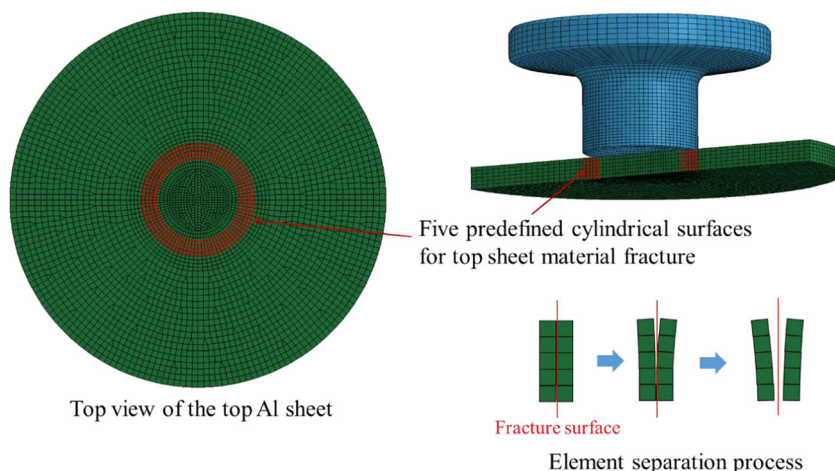
3 Results and discussion

3.1 Model validation

Finite element solution of the abovementioned model was obtained using LS-DYNA solver. Process parameters used in the model included a feed rate of 1.35 mm/s and a spindle speed of 900 rpm. A feed depth of 4.3 mm was defined such that the process terminated with the bottom edge of the rivet head touched the surface of the top sheet. Parallel physical tests were conducted to validate the model [14].

Fig. 2 Geometry, mesh, and mechanical boundary conditions of the F-SPR model. **a** Cross-section view of the entire model. **b** Boundary condition of the rivet. **c** Boundary condition of the sheets
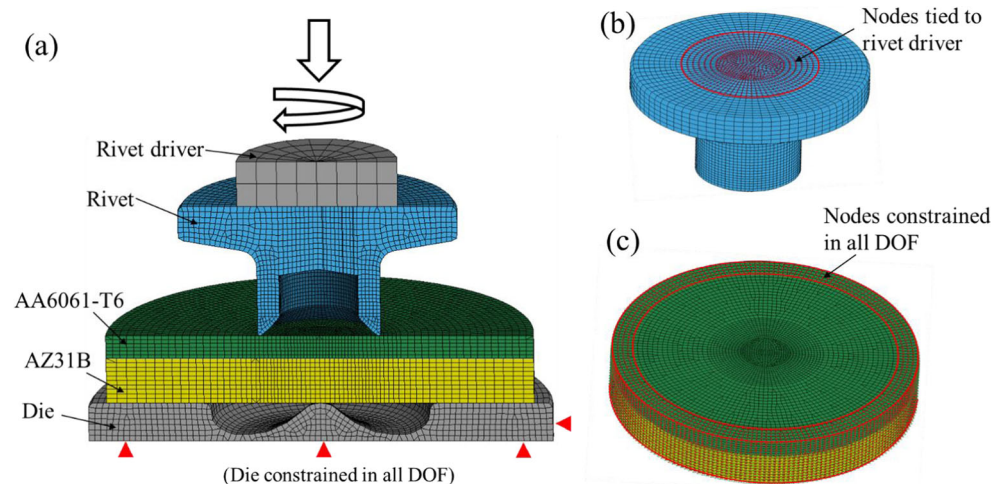
Fig. 3 Locations of the predefined fracture surfaces on top sheet and the schematic of element separation process

Five predefined cylindrical surfaces for top sheet material fracture

Top view of the top Al sheet

Fracture surface

Element separation process

The experimental and simulated joint profiles were compared in terms of rivet shank flaring, remaining thickness, and shank length in the final joint (refer to Fig. 4). The simulated shank flaring value was a bit smaller than that of the experimental one, but the simulated remaining thickness and deformed shank length were larger than the experimental ones. This is assumed to result from the material properties of the steel rivet, which was obtained indirectly with the help of hardness measurement results. The material softening of the steel rivet at elevated temperatures would probably be underestimated; therefore, the simulated rivet was a bit stiffer than the experimental one. A stiffer rivet shank material would therefore resulted in smaller rivet shank flaring and less upsetting. As the largest difference between simulation and experiment was 13.1%, the simulation accuracy was still acceptable.

3.2 Joint formation process

F-SPR is more like a material forming process, during which localized plastic deformations of materials are introduced by
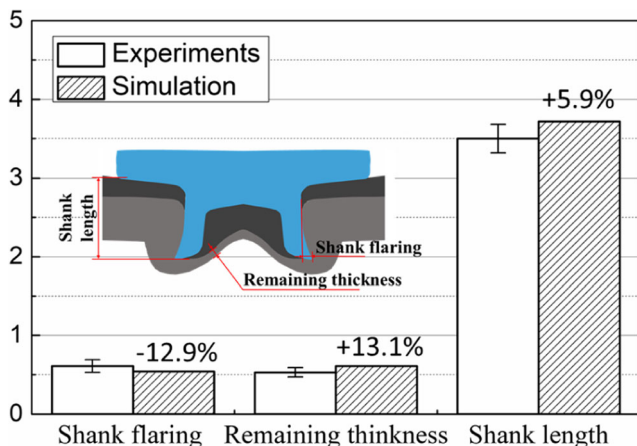

Fig. 4 Geometrical feature comparison of experimental and simulated F-SPR joints

the moving rivet and the static die. The localized plastic deformation of sheet material, which also appears in traditional SPR process, are the causation of cracking in Mg sheet. Therefore, in order to understand how the plastic deformation evolves and the locations that cracking is apt to occur, the deformation and strain histories of the F-SPR joint were investigated based on the validated numerical model. Figures 5 and 6 show, respectively, the effective plastic strain distribution of the workpieces and the rivet during F-SPR process at four different stages with a time interval of 0.8 s.

At the beginning of the process, the spinning rivet was brought to contact with the top sheet, and large plastic deformations appeared in the top Al material near the rivet shank tip and in the bottom Mg material that contacting with the die (refer to the geometry of 0.8 s in Fig. 5). With the ongoing downward movement of the rivet, the sheets were further deformed to gradually form the shape of the die profile. In the final joint, the top sheet was penetrated through by the rivet and an obvious large deformation region, with the diameter of about 6.8 mm, was observed in the center of the bottom sheet (refer to the geometry of 3.185 s in Fig. 5). Because of the low-ductility nature of Mg sheet, which makes it easier to crack during traditional SPR process, the appearance of the large deformation region indicates that the materials in this region are at a risk of cracking. Therefore, the improvement of formability of the Mg material in this region is of great importance for cracking inhibition during the F-SPR process.

For the rivet, however, the evolution of plastic deformation was quite different from that of the workpieces. Only very localized plastic deformation at the rivet shank tip appeared before 2.4 s and the rivet shank flared slightly (refer to the geometries of 0.8, 1.6, and 2.4 s in Fig. 6). In the final one quarter period of the process, the large plastic strain region expanded abruptly from the shank tip towards the rivet head and an obvious shank flaring occurred (refer to the geometry of 3.185 s in Fig. 6). This is because before 2.4 s, a relative large portion of the die was left empty, resulting in a relative
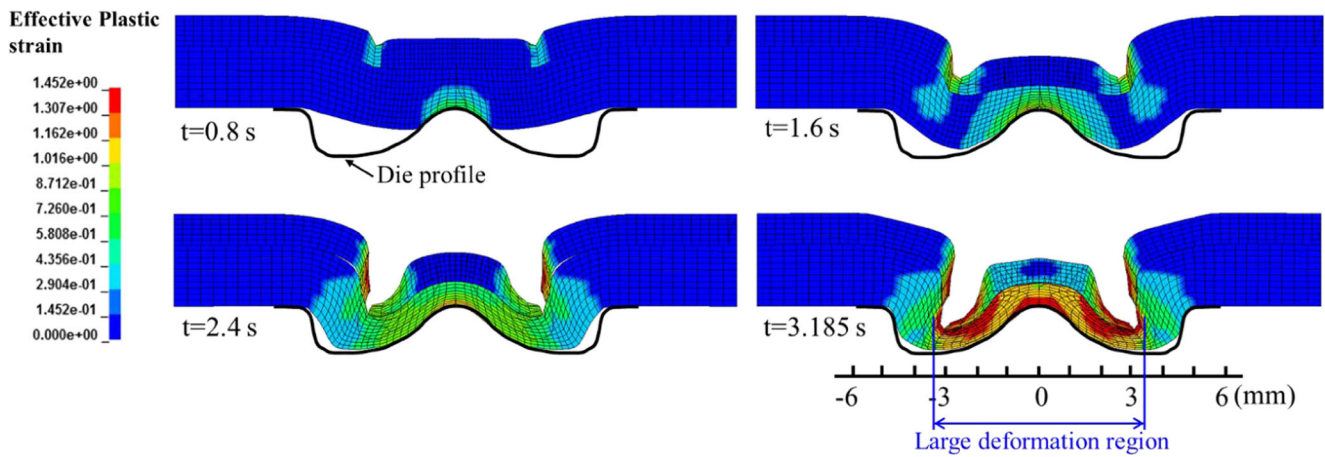
Fig. 5 Cross-section geometry evolution and effective plastic strain distributions of the Al and Mg workpieces during F-SPR process

small axial force and the rivet deformed slightly (refer to the geometry of 2.4 s in Fig. 5). After 2.4 s, the die was almost fully filled by the displaced sheet materials (refer to the geometry of 3.185 s in Fig. 5) as a result of which large squeezing force was applied to the materials locating in between the rivet shank tip and the valley of the die. Therefore, large localized plastic deformation appeared in the bottom Mg sheet and the rivet shank flared severely.

Different from the solid pin in friction stir spot welding process, the F-SPR rivet has a semi-tubed shank, which could contain the displaced workpiece materials in it during the F-SPR process. Based on this feature, after the top sheet was penetrated through by the rotating rivet, i.e., after complete failure of the preset crack surface on the top sheet occurred, the cutoff portion of the top sheet was contained inside the rivet shank cavity and no longer connected to the rest portion of the top sheet. To show the moving condition of the cutoff portion of the top sheet, four tracing nodes were selected. Points A, B, and C are located inside the preset crack surfaces, i.e., in the cutoff portion, and point D was outside the preset crack surfaces, i.e., in the outer portion of the top sheet. Figure 7 shows the history plots of X-coordinates of the four nodes.

Obviously, the X-coordinates of points A, B, and C changed slightly in the beginning period of the process, indicating a small in-plane deformation occurred to the inner portion of the top sheet. After the process time of 1.82 s, the X-coordinates of these three points started to change periodically with the magnitudes of around 1.8 mm and the periods of 0.44 s, indicating the occurrence of rotation of the cutoff portion. In addition, the similar magnitudes and periods of the three points indicated that the cutoff portion did not had an obvious in-plane twist and rotated as a whole part until the end of the process. However, point D kept static throughout the process, evidenced by its almost unchanged X-coordinate. Since the rotation of the cutoff portion was 0.44 s, smaller than that of the rivet, which was 0.067 s at a spinning speed of 900 rpm, the cutoff portion did not stick to the rivet and relative motion still existed at the rivet/cutoff portion as well as the cutoff portion/bottom sheet interfaces.

3.3 Temperature features

Temperature distribution of the rivet and sheet materials at the four specific moments are given in Fig. 8. It is interesting that the highest temperature was concentrated at the

Fig. 6 Cross-section geometry evolution and effective plastic strain distribution of the rivet during F-SPR process
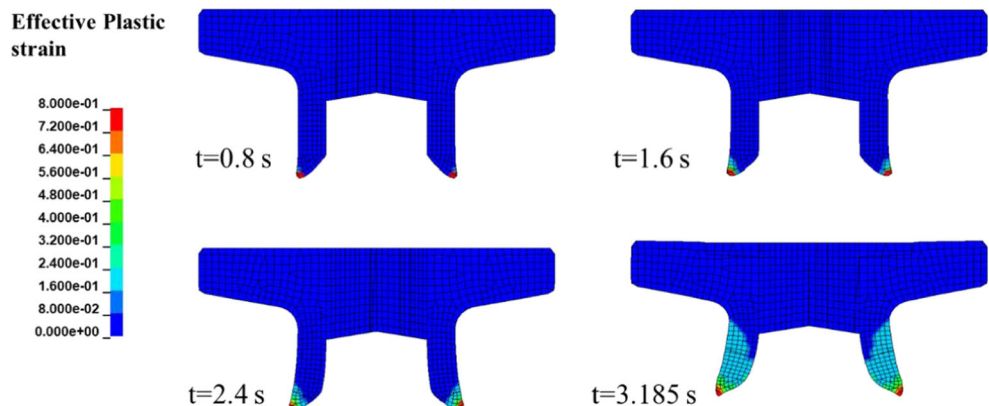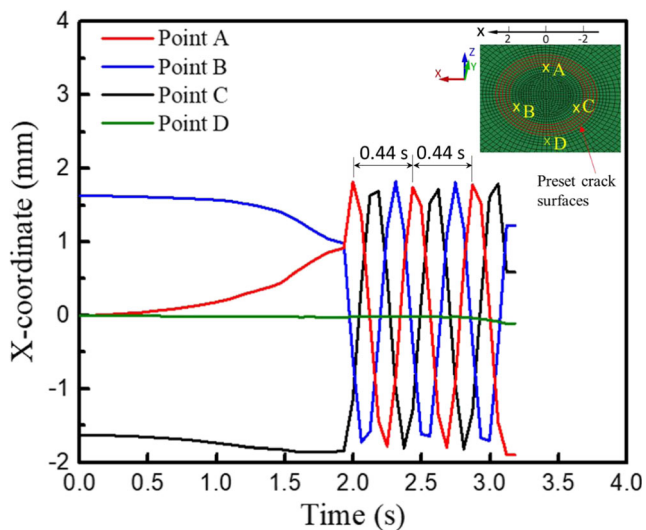
Fig. 7 History plots of *X*-coordinates of the four selected nodes during F-SPR process

rivet shank tip during the first three quarters of the process (refer to the figures of 0.8, 1.6, and 2.4 s in Fig. 8) and expanded a bit along the rivet shank in the final one quarter of the process (refer to the figure of 3.185 s in Fig. 8). This is because the rivet shank flared slightly in the first three quarters of the process; therefore, larger contact pressure was concentrated at the rivet/workpiece interface near the rivet shank tip, and as a result, relative larger portion of the frictional heat was generated at the rivet shank tip. When the rivet shank flared greatly in the final one quarter of the process, the pressure at the rivet/workpiece contact interface locating inside the rivet shank cavity started to increase, resulting in the increase of generated frictional heat inside the rivet shank cavity.

It should be noted that the thermal contours at the top sheet/bottom sheet interface were discontinuous (refer to the figures of 1.6, 2.4, and 3.185 s in Fig. 8). This can be explained by two reasons. One is gap formation in between the two layers of sheets due to the different bending patterns of the sheets and material failure of the top sheet during the simulated process

(refer to Fig. 9). These gaps introduced additional contact thermal resistance to the interface of the sheets and thus resulted in the discontinuous temperature at the interface. Another reason is the rotation of the cutoff portion of the top sheet, which created additional heat generation at the cutoff portion/bottom sheet interface.

To investigate the temperature evolution of rivet and sheets during the F-SPR process, three specific nodes locating on the rivet shank tip, the top Al sheet, and the bottom Mg sheet, respectively, were selected. Figure 10 shows the location and the temperature evolution of the three selected nodes. The temperature-time curves can be divided into three phases representing, respectively, the piercing, expanding, and upsetting phases. The dividing line between the piercing and expanding phases corresponded to the moment the top sheet was pierced through by the rotating rivet, before which frictional heat was only generated at the rivet/top sheet contact interfaces, i.e., along the rivet side interface on both sides. After this moment, frictional heat was generated at the rivet/top sheet contact interface, the rivet/bottom sheet interface, and the cutoff portion/bottom sheet interface based on the local contact pressure. The dividing line between the expanding and upsetting phases corresponded to the moment that the bottom sheet touched the lowermost point of the die, which was featured by the sudden increase of the axial riveting force during the F-SPR process.

Obviously, the temperature evolution at these three locations differed significantly from each other. The temperature of point 1 (on the rivet) kept raising throughout the process for the increasing amount of generated frictional heat at the rivet shank tip and reached its peak of 580 °C, at the end of the process. The temperature of point 2 (on the top sheet) reached its peak of 380 °C at the end of the piercing stage and then began to decrease. However, for point 3 (on the bottom sheet), its temperature increased monotonically at a lower rate compared to point 2 and a peak temperature of 220 °C was reached at the end of the whole process.

Fig. 8 Temperature distribution during the F-SPR process
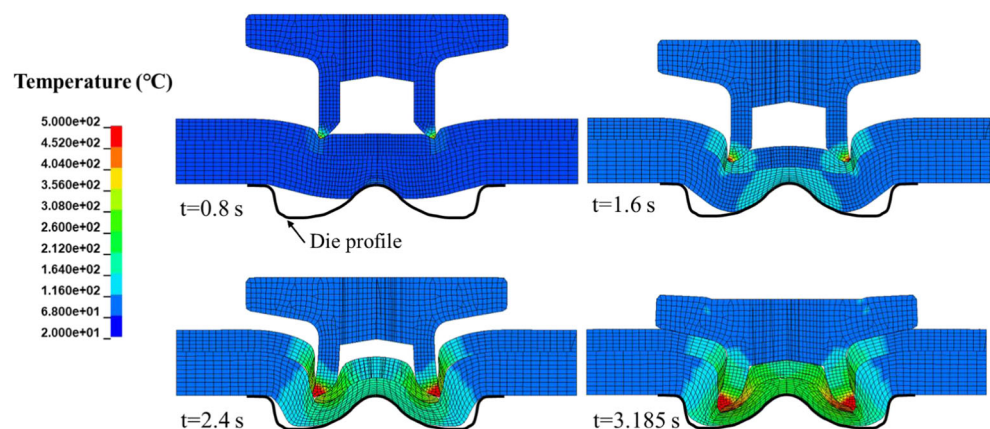
Fig. 9 Gap formation in between the two layers of sheets at the simulation time of 2.5 s
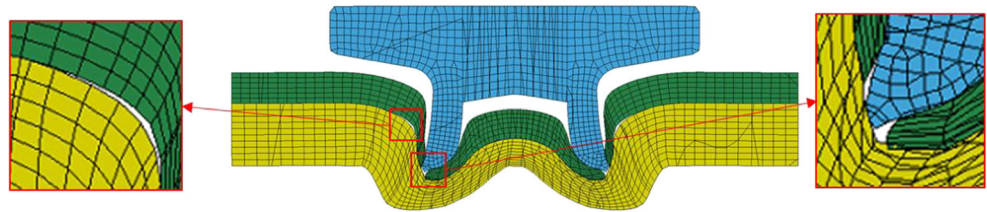
The different temperature evolution profiles of point 2 and point 3 can be explained by the dynamically changing contact conditions between the rivet and the sheets throughout the F-SPR process. At the very beginning, the rivet touched the top sheet, and the temperature of point 2, which is located in the top sheet, increased as a result of the increased amount of frictional heat generated between the rivet and the top sheet. However, for point 3, which is located on the bottom sheet, as there was almost no relative motion between the top and bottom sheets, no frictional heat was produced. The heat sources of the bottom sheet were heat conduction from the top sheet, which was in dominant, and heat generation from local plastic deformation, which took a relative smaller part of the total heat generation. Therefore, during the piercing phase, the temperature of point 3 increased at a lower rate than that of point 2.

After the top sheet was penetrated through by the rivet, the contact pressure between the rivet and the top sheet decreased; therefore, the frictional heat generation at rivet/top sheet decreased accordingly. As there was still temperature gradient between top sheet and bottom sheet, heat conduction from top sheet to bottom sheet continued; therefore, the temperature of point 2 reached its peak value and began to drop. However, for point 3, as the top sheet was penetrated through, the rivet tip started to contact with the bottom sheet directly and frictional heat was generated on the rivet/bottom sheet interface. In

addition, frictional heat generation introduced by the rotating cutoff portion of the top sheet also provided additional heat source to the workpieces. Therefore, the temperature of point 3 kept rising at a higher rate. At about 3.05 s, the bottom sheet expanded to its largest extent, the rivet began to upset, and the contact pressure between the rivet and the bottom sheet increased abruptly, as a result of which more frictional heat was produced and the temperature of point 3 increased at an even higher rate.

### 3.4 Effects of spindle speed on cracking inhibition

To investigate the influence of spindle speeds on the heating temperature of bottom Mg sheet in the final F-SPR joint, the F-SPR processes under the same feed rate of 1.35 mm/s, but different spindle speeds, i.e., 900, 1450, and 2000 rpm, were simulated. The temperature distributions along the radial direction on the surface of the bottom sheet under different spindle speeds are shown in Fig. 11.

Obviously, the temperature distributions under different spindle speeds had a similar tendency with the peak values that appeared at about 2.5 mm away from the sheet center. With the increase of the spindle speed, the temperatures raised as a result of the increased amount of generated frictional heat. It is interesting that the sheet materials in the large deformation

Fig. 10 Temperature evolution of three typical points locating on the rivet, the top sheet, and the bottom sheet
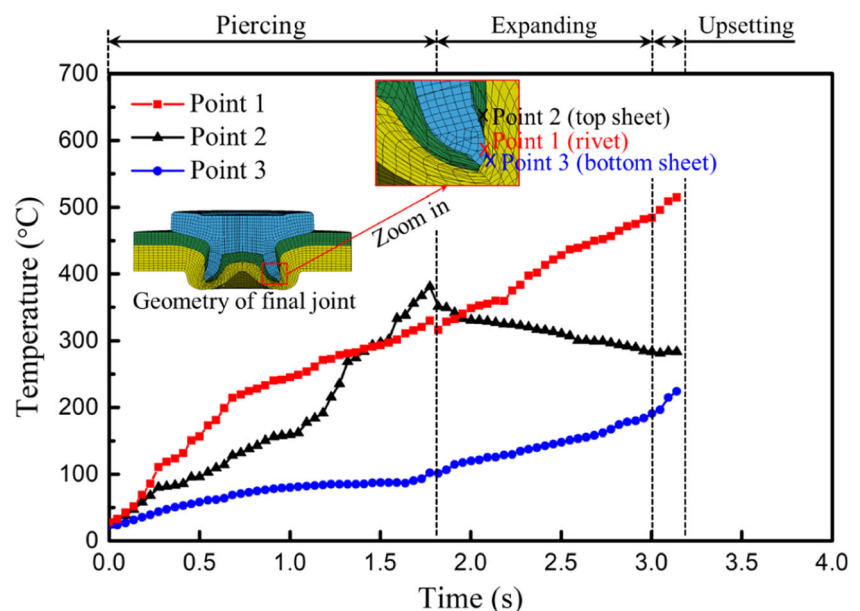
Fig. 11 Surface temperature distribution of the bottom sheet along the radial direction at the end of the F-SPR process
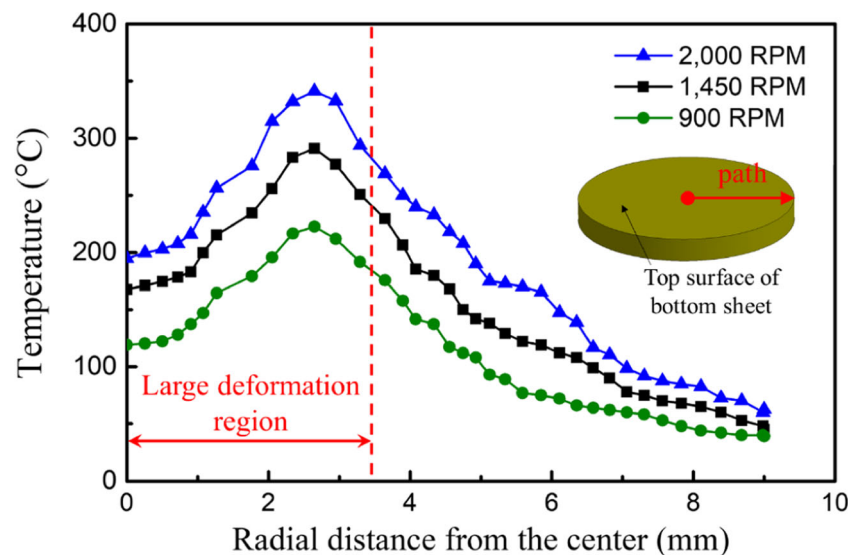

region, which was marked with a diameter of about 6.8 mm in Fig. 5, were heated to a relative higher temperature. One reason of this local high temperature is the maximum rate of frictional heat generation at the rivet shank tip, which has a radius of 2.65 mm, due to the presence of maximum tangential velocity and contact pressure. Another reason is the greater amount of heat produced by the larger plastic deformation in this region. Thus, the dangerous zones that were prone to cracking, i.e., the larger deformation regions, were heated to relative higher temperatures, which contributed to the improvement of the material ductility in these regions to inhibit cracking. This can be recognized as the local heating effect of the F-SPR process.

Wang et al. [12] pointed out that a preheating temperature of above 180 °C could help eliminate cracking in the SPRed Mg joints and increase the joint strength significantly. It can be seen from Fig. 11 that when a spindle of 1450 rpm was

applied, the lowest temperature in the large deformation region was about 168 °C, and the spindle speed of 2000 rpm could result in the temperature of over 194 °C in the large deformation region. Therefore, it is reasonable to predict from the simulation results that cracking in the large deformation region can be eliminated when the spindle speed is above 2000 rpm. To validate this prediction, parallel physical tests of the F-SPR process were conducted using the same sets of process parameters. Figure 12 shows the cross-section profiles and bottom appearances of the F-SPR joints under the feed rate of 1.35 mm/s and the spindle speeds of 900, 1450, and 2000 rpm.

When the spindle speed was 900 rpm, some large cracking could be observed both inside the joint and on the bottom surface (refer to Fig. 12(a), (a')). When the spindle speed increased to 1450 rpm, there were only a few small cracking near the rivet shank tip and large cracking could still be observed on the bottom surface (refer to Fig. 12(b), (b')). When
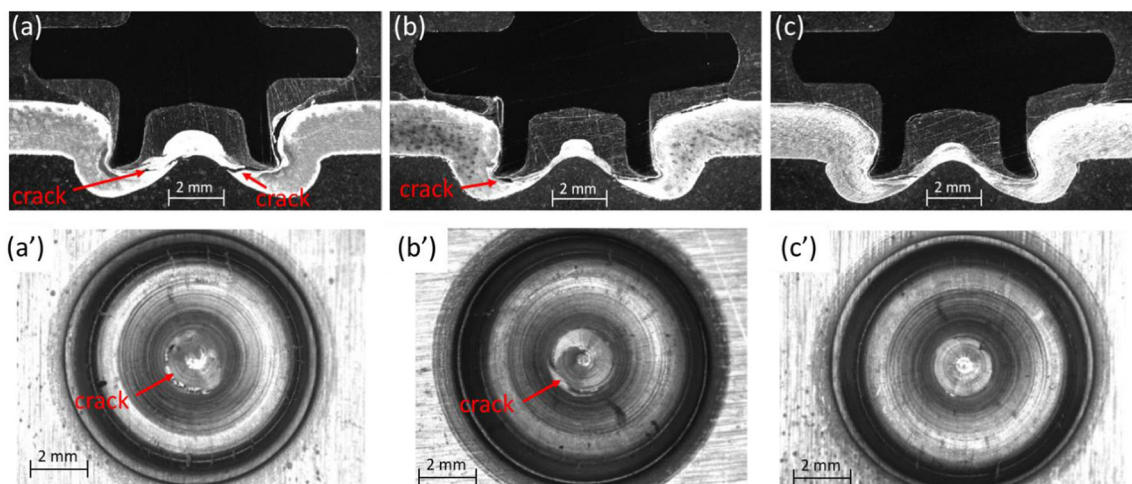
Fig. 12 Cross-section profiles and bottom appearances of the F-SPR joints under the same feed rate of 1.35 mm/s and different spindle speeds. (a), (a') 900 rpm. (b), (b') 1450 rpm. (c), (c') 2000 rpm

the spindle speed increased to 2000 rpm, no cracking could be observed (refer to Fig. 12(c), (c')), which was in accordance with the numerical predictions. To this end, the prediction accuracy of the proposed numerical model is further validated.

4 Conclusions

A coupled thermal-mechanical model based on solid mechanics has been proposed and validated to simulate the F-SPR process taking into consideration the temperature and strain rate-dependent material properties. The following conclusions are drawn:

(1) The proposed numerical model of F-SPR process achieved good correlations in geometry profile with parallel physical test results byintegrating Johnson-Cook material model, interface frictional heat generation, preset crack surface method, and ignoring the sticking contact condition.

(2) During F-SPR process, the central portion of the top sheet was cut off by the rivet and rotated along its symmetry axis creating additional frictional heat generation at the interface of workpieces inside the rivet shank.

(3) Rivet and sheet materials underwent different local thermal histories during the F-SPR process due to the complex contact and heat generation conditions. The temperature of the rivet and the bottom sheet kept raising throughout the process, while the temperature of top sheet reached its peak before being pierced through by the rivet and then decreased gradually.

(4) At a fixed feed rate of 1.35 mm/s, the final temperature in the large deformation region of an F-SPR joint increased with the increase of spindle speed from 900 to 2000 rpm. The final temperature of larger than 194 °C could be achieved in the large deformation region of bottom Mg sheet with a spindle speed of 2000 rpm, under which condition cracking in the F-SPR joint could be eliminated.

References

1. Figner G, Vallant R, Weinberger T, Enzinger N, Schröttner H, Paśič H (2013) Friction stir spot welds between aluminium and steel automotive sheets: influence of welding parameters on mechanical properties and microstructure. Welding in the World 53(1–2):R13–R23

2. Liu L, Ren D, Liu F (2014) A review of dissimilar welding techniques for magnesium alloys to aluminum alloys. Materials (Basel) 7(5):3735–3757

3. Sigler DR, Carlson BE, Janiak P (2013) Improving aluminum resistance spot welding in automotive structures. Weld J 92(6):64–72

4. Qi X-d, Liu L-m (2012) Fusion welding of Fe-added lap joints between AZ31B magnesium alloy and 6061 aluminum alloy by hybrid laser–tungsten inert gas welding technique. Mater Des 33: 436–443

5. Hayat F (2011) The effects of the welding current on heat input, nugget geometry, and the mechanical and fractural properties of resistance spot welding on Mg/Al dissimilar materials. Mater Des 32(4):2476–2484

6. Sun M, Behravesh SB, Wu L, Zhou Y, Jahed H (2017) Fatigue behaviour of dissimilar Al 5052 and Mg AZ31 resistance spot welds with Sn-coated steel interlayer. Fatigue & Fracture of Engineering Materials & Structures 40(7):1048–1058

7. He X, Zhao L, Deng C, Xing B, Fengshou G, Ball A (2015) Self-piercing riveting of similar and dissimilar metal sheets of aluminum alloy and copper alloy. Materials & Design (1980–2015) 65:923–933

8. Mori K, Abe Y, Kato T (2014) Self-pierce riveting of multiple steel and aluminium alloy sheets. J Mater Process Technol 214(10): 2002–2008

9. Ma YW, Lou M, Li YB, Lin ZQ (2018) Effect of rivet and die on self-piercing rivetability of AA6061-T6 and mild steel CR4 of different gauges. J Mater Process Technol 251:282–294

10. Luo AA, Lee TM, Carter JT (2011) Self-pierce riveting of magnesium to aluminum alloys. SAE International Journal of Materials and Manufacturing 4(1):158–165

11. Durandet Y, Deam R, Beer A, Song W, Blacket S (2010) Laser assisted self-pierce riveting of AZ31 magnesium alloy strips. Mater Des 31(SUPPL. 1):S13–S16

12. Wang JW, Liu ZX, Shang Y, Liu AL, Wang MX, Sun RN, Wang P-C (2011) Self-piercing riveting of wrought magnesium AZ31 sheets. J Manuf Sci Eng 133(3):031009

13. Jäger A, Lukáč P, Gärtnerová V, Bohlen J, Kainer KU (2004) Tensile properties of hot rolled AZ31 Mg alloy sheets at elevated temperatures. J Alloys Compd 378(1–2):184–187

14. Li YB, Wei ZY, Wang ZZ, Li YT (2013) Friction self-piercing riveting of aluminum alloy AA6061-T6 to magnesium alloy AZ31B. J Manuf Sci Eng 135(6):061007

15. Ma Y, Lou M, Yang Z, Li Y (2015) Effect of rivet hardness and geometrical features on friction self-piercing riveted joint quality. J Manuf Sci Eng 137(5):054501

16. Liu X, Lim YC, Li Y, Tang W, Ma Y, Feng Z, Ni J (2016) Effects of process parameters on friction self-piercing riveting of dissimilar materials. J Mater Process Technol 237:19–30

17. Ma YW, Li YB, Wei H, Lou M, Lin ZQ (2016) Modeling of friction self-piercing riveting of aluminum to magnesium. J Manuf Sci Eng 138(6):061007

18. Min J, Li J, Carlson BE, Li Y, Quinn JF, Lin J, Wang W (2015) Friction stir blind riveting for joining dissimilar cast Mg AM60 and Al alloy sheets. J Manuf Sci Eng 137(5):051022

19. Han G, Wang M, Liu Z, Wang P-C (2013) A new joining process for magnesium alloys: rotation friction drilling riveting. J Manuf Sci Eng 135(3):031012

20. Zhang XX, Xiao BL, Ma ZY (2011) A transient thermal model for friction stir weld. Part I: the model. Metall Mater Trans A 42(10): 3218–3228

21. Nandan R, Roy GG, Lienert TJ, Debroy T (2007) Three-dimensional heat and material flow during friction stir welding of mild steel. Acta Mater 55(3):883–895

22. Johnson GR, Cook WH (1983) A constitutive model and data for metals subjected to large strains, high strain rates and high temperatures. in Proc. 7th Int. Symp. on Ballistics

23. Al-Badour F, Merah N, Shuaib A, Bazoune A (2013) Coupled Eulerian Lagrangian finite element modeling of friction stir welding processes. J Mater Process Technol 213(8):1433–1439

24. Ulacia I, Salisbury CP, Hurtado I, Worswick MJ (2011) Tensile characterization and constitutive modeling of AZ31B magnesium alloy sheet over wide range of strain rates and temperatures. J Mater Process Technol 211(5):830–839

25. Zhang C, Ma G, Nie J, Ye J (2015) Numerical simulation of AZ31B magnesium alloy in DE-GMAW welding process. Int J Adv Manuf Technol 78(5–8):1259–1264

26. Gao Z, Niu JT, Krumphals F, Enzinger N, Mitsche S, Sommitsch C (2013) FE modelling of microstructure evolution during friction stir spot welding in AA6082-T6. Welding in the World 57(6):895–902

27. Livermore Software Technology Corporation (2016) LS-DYNA keyword user's manual, volume 1, version r7598. p. 635

28. Liu X, Lan S, Ni J (2015) Thermal mechanical modeling of the plunge stage during friction-stir welding of dissimilar Al 6061 to TRIP 780 steel. J Manuf Sci Eng 137(5):051017

29. Khandkar MZH, Khan JA, Reynolds AP (2013) Prediction of temperature distribution and thermal history during friction stir welding: input torque based model. Sci Technol Weld Join 8(3):165–174